JOURNAL OF GEOPHYSICAL RESEARCH, VOL. 113, A03103, doi:10.1029/2007JA012733, 2008

Electron temperature anisotropy constraints in the solar wind

Štěpán Štverák,[1,3] Pavel Trávníček,[1,2] Milan Maksimovic,[3] Eckart Marsch,[4] Andrew N. Fazakerley,[5] and Earl E. Scime[6]

Received 16 August 2007; revised 9 October 2007; accepted 15 November 2007; published 19 March 2008.

[1] We have performed a statistical study of a substantial amount of electron data acquired in the solar wind to understand the constraints on electron temperature anisotropy by plasma instabilities and Coulomb collisions. We use a large data set of electron measurements from three different spacecraft (Helios I, Cluster II, and Ulysses) collected in the low ecliptic latitudes covering the radial distance from the Sun from 0.3 up to 4 AU. We estimate the electron temperature anisotropy using fits of the measured electron velocity distribution functions acquired in situ. We use a two population (core and halo) analytical model and properties of both populations are studied separately. We examine all the acquired data in terms of temperature anisotropy versus parallel electron plasma beta, and we relate the measurements to the growth rates of unstable modes. The effect of Coulomb collisions is expressed by the electron collisional age A_e defined as the number of collisions suffered by an electron during the expansion of the solar wind. We show that both instabilities and collisions are strongly related to the isotropisation process of the electron core population. In addition we examine the radial evolution of these effects during the expansion of the solar wind. We show that the bulk of the solar wind electrons are constrained by Coulomb collisions, while the large departures from isotropy are constrained by instabilities.

Citation: Štverák, Š., P. Trávníček, M. Maksimovic, E. Marsch, A. N. Fazakerley, and E. E. Scime (2008), Electron temperature anisotropy constraints in the solar wind, *J. Geophys. Res.*, *113*, A03103, doi:10.1029/2007JA012733.

1. Introduction

[2] The solar wind is a weakly or almost collisionless medium. For electrons at 1 AU the mean free path is of order 10^8 km, comparable with the typical length scales of the system. As expected, solar wind electrons are found to be out of the thermodynamic equilibrium. Beside the thermal core, the electron velocity distribution functions (eVDF) exhibit two nonthermal features: suprathermal tails known as the halo population and a magnetic field-aligned strahl moving in the antisunward direction [*Feldman et al.*, 1975; *Rosenbauer et al.*, 1977; *Pilipp et al.*, 1987a]. What is the origin of such distributions and more generally what are the physical processes that transport the energy in the solar wind? These questions are still a matter of considerable discussion [*Marsch*, 2006].

[3] In the absence of some mechanisms for interchange of the parallel and perpendicular pressure, the application of the classical CGL relations [*Chew et al.*, 1956] to the solar wind electrons expanding in the spiral structured interplanetary magnetic field predicts large temperature anisotropies. Starting with an isotropic electron distribution close to the Sun, this simple model predicts, for a typical slow solar wind at 1 AU, a temperature ratio between the parallel $T_{\parallel}$ and perpendicular $T_{\perp}$ temperature (the directions are with respect to the ambient magnetic field) of more than 30 [*Phillips and Gosling*, 1990]. However, the observed solar wind at this distance is found much closer to the isotropic state with an average $T_{\parallel}/T_{\perp}$ of 1.2 [*Feldman et al.*, 1975; *Pilipp et al.*, 1987b]. In order to explain these observations some physical processes that can effectively transfer the internal kinetic energy of the solar wind electrons from the parallel to the perpendicular directions are needed to counteract the adiabatic expansion and thereby maintain the plasma close to the isotropic state. There are three main kinetic processes able to cause these effects: electron instabilities driven by temperature anisotropy, Coulomb collisions, and heat-flux skewness.

[4] Sufficiently large temperature anisotropies can drive electromagnetic fluctuations. The more we cross the instability threshold, the larger are field fluctuations caused by the given instability. In turn, these fluctuations isotropize the

[1]Institute of Atmospheric Physics, Academy of Sciences of the Czech Republic, Prague, Czech Republic.
[2]Astronomical Institute, Academy of Sciences of the Czech Republic, Prague, Czech Republic.
[3]Laboratoire d'Etudes Spatiales et d'Instrumentation en Astrophysique, Observatoire de Paris, Centre National de la Recherche Scientifique, Université Pierre et Marie Curie, Université Paris Diderot, Meudon, France.
[4]Department for Sun and Heliosphere, Max Planck Institute for Solar System Research, Katlenburg-Lindau, Germany.
[5]Mullard Space Science Laboratory, University College London, Dorking, UK.
[6]Department of Physics, West Virginia University, Morgantown, West Virginia, USA.

0148-0227/08/2007JA012733$09.00

Table 1. Data Set Used in This Study Including Data From Three Spacecraft: Helios I, Cluster II, and Ulysses[a]

Spacecraft	Instrument	Period	Distance, AU	Samples
Helios 1	I2	1975–1978	0.3–1.0	~100,000
Cluster II	PEACE	2002–2003	1.0	~10,000
Ulysses	SWOOPS	1990–1991	1.2–3.95	~14,000

[a]Data set includes roughly 125,000 samples covering the radial distances from the Sun from 0.3 up to 4 AU.

distribution function via wave-particle scattering. The anisotropy driven instabilities therefore place constraints on the temperature anisotropy $T_\perp/T_\parallel$ itself. The unstable modes can be derived from the linear Vlasov theory. For the purpose of this study we consider two main electron temperature anisotropy driven instabilities. The first type arises when the perpendicular electron temperature is greater than the parallel one ($T_\perp/T_\parallel > 1$). For an electron population described by a single bi-Maxwellian distribution and for a sufficiently homogeneous plasma, the fastest-growing instability caused by this anisotropy is the whistler [*Kennel and Petscheck*, 1966; *Dum et al.*, 1980]. Electrons are cyclotron resonant with whistler waves while protons are not; thus the proton temperature has no effect on the properties of this instability. In the opposite case when $T_\perp/T_\parallel < 1$ the electron fire hose instability evolves [*Hollweg and Volk*, 1970]. The most dominant mode of this type of instability is the oblique propagating fire hose [*Paesold and Benz*, 1999; *Li and Habbal*, 2000]. In this case the protons are resonant with the electron mode so that the maximum growth rate for this instability is also a function of the proton temperature. The effect of proton temperature anisotropy driven instabilities on the temperature anisotropy has already been studied in detail by *Kasper et al.* [2003], *Hellinger et al.* [2006], and *Marsch et al.* [2006] for the solar wind protons. Those authors have shown fairly good agreement between the linear theory predictions and a large amount of Wind/SWE and Helios observations. Some studies of this kind have been already done for the electrons. *Gary et al.* [1999] and *Phillips et al.* [1989] have shown that the solar wind electrons are typically stable to these instabilities. The purpose of this paper is to perform a statistical study on the solar wind electrons which is similar to the study by *Hellinger et al.* [2006] on the protons. Our study is performed for a large variety of different solar wind plasmas.

[5] Even though Coulomb collisions in the solar wind are unfrequent, some studies suggest that they can still affect the isotropization processes. Specially for denser and colder plasmas [*Livi et al.*, 1986], the collision frequency is increased and the electron Coulomb collisions can become important. It was shown by *Phillips et al.* [1989] that the electron temperature anisotropy is well correlated with density. In denser plasmas the electrons are mostly found closer to the isotropic state. Another and more sophisticated way to compare the collisions with the anisotropy was presented by *Salem et al.* [2003]. *Salem et al.* [2003] computed the electron collisional age A_e defined as a most probable number of collisions suffered by an electron during the expansion of the solar wind. In other words, A_e expresses how collisionaly old the plasma is at the moment of the measurement. Their results are again in agreement with the expectation that the collisionally older the plasma is the less anisotropic it is. Since our data were acquired at different radial distances, we have also used the concept of collisional age A_e. Note, however, that this concept does not apply to the trapped electrons that circle on closed magnetic field lines [*Bame et al.*, 1981; *Gosling et al.*, 1987].

[6] The aim of the present study is to explore, for a large amount of observed eVDF and a wide range of heliocentric distances, the combined effect of the plasma instabilities and the the collisions on the temperature isotropization. In section 2 we briefly describe the data we have used for our study and some basic facts about the instruments used for their acquisition. Section 3 presents the theoretical eVDF model we have used in our study and explains the data analysis method. All the results are then presented and discussed in section 4. A brief summary and concluding remarks are given in section 5.

2. Data

[7] The data set used in our study includes eVDFs measured on board three spacecraft: Helios I, Cluster II (Samba), and Ulysses. We have analyzed roughly 120,000 data samples covering the radial distances from 0.3 up to 4 AU; see Table 1. All data were collected in low ecliptic latitudes during both solar cycles, the solar minimum (Helios I data from 1975 to 1977) and the solar maximum (the rest of the data).

[8] The Helios I spacecraft (see *Porsche* [1975] for general information) was launched in 1974 into an ecliptic orbit with a perihelion around 0.3 AU. The probe continuously spun around an axis oriented perpendicular to the ecliptic plane. The solar wind electrons were measured by an electron analyzer placed in the equatorial plane with a field of view oriented perpendicular to the spin axis [*Schwenn et al.*, 1975]. By use of the spacecraft rotation, the electron flux was measured in eight angular bins spaced 45° apart with polar and azimuthal field of view of 19° and 28.1°, respectively. The energy range from 0.5 to 1660 eV was covered in 32 energy channels, 16 for the low-energy mode (up 15.5 eV) and the same number of channels for the high-energy mode (10.69 to 1658 eV). The measurements were acquired typically with a time resolution of 40 s. Since in our study we need to analyze eVDFs measured in the $v_\perp$, $v_\parallel$ plane, we use only data samples where the magnetic field vector is close to the ecliptic plane, that is when $B_z/|B| < 0.1$, thus the angle between the interplanetary magnetic field vector and the ecliptic plane is less then $\approx 6°$. Figure 1 shows one sample of such a measurement. Asterisks represent measured energy channels in the eight angular directions and the grayscale represents linearly interpolated values (used for presentation purpose only) of the distribution. The velocity components, in which the data are produced, are the radial direction from the sun v_R and the tangential direction in the ecliptic plane v_T. These components are transformed to $v_\perp$, $v_\parallel$ by use of the measured ambient magnetic field (black arrow in Figure 1).

[9] The four satellites of the Cluster II mission [*Escoubet et al.*, 1997] were launched in 2000 on elliptical polar orbits with a maximum distance of 19.6 R_E from the Earth. The satellites thus spend only a small part of their orbits in front

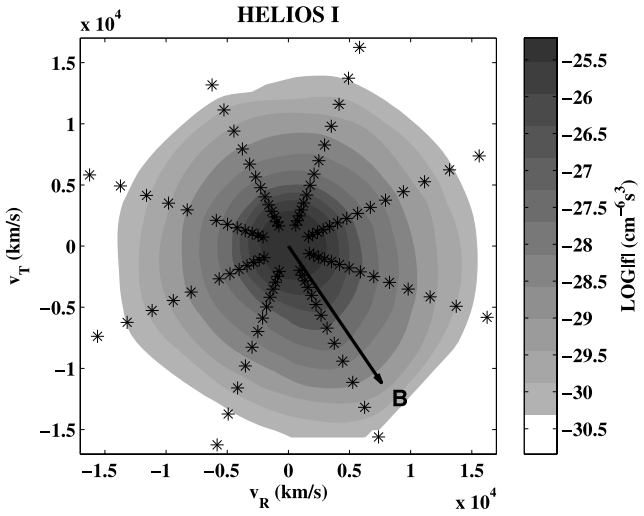

Figure 1. Example of measured electron distribution by the electron analyzer on board Helios I. The asterisks represent the measured energy bins and the black arrow shows the direction of the interplanetary magnetic field. For presentation purpose the measured values are interpolated to a grayscale map.

of the Earth's bow shock in the unperturbed solar wind. The eVDFs on board the Cluster satellites are measured with the PEACE instrument [*Johnstone et al.*, 1997]. The PEACE instrument consists of two similar electron analyzers (LEEA and HEAA) placed oppositely on the spacecraft body. By use of the satellite spin, a full solid angle is covered by this instrument. Each of the analyzers has 12 polar sectors covering the full π angle with a azimuthal field of view of 2° and 5.2° for LEEA and HEEA, respectively. The full energy scale for both instruments ranges from 0.6 eV to 26.5 keV. There are several modes on the instrument that differ in number of energy levels and used angular resolution. Herein we have used the SPINPAD data product which provides two-dimensional (2-D) eVDFs covering one half of the ($v_\perp$, $v_\parallel$) plane in 13 angular bins with time resolution of 4 s (which is the spin period). Since the spacecraft spend most of the time in the Earth's magnetosphere we had to correctly select only periods when the satellite was in the unperturbed solar wind plasma not magnetically connected to the Earth's bow shock. Such an example of a SPINPAD product is shown on Figure 2 where the asterisks represents again the measured angular and energy bins and the grayscale map the interpolated values.

[10] The Ulysses spacecraft, launched in 1990, was designed to study the solar wind properties in all solar latitudes. To reach them, the satellite first traveled in the ecliptic to Jupiter in order to use its high gravitational assist to accelerate to higher solar latitudes. Only data from this first part of the mission were used here. On board Ulysses the eVDFs are measured by the SWOOPS instrument [*Bame et al.*, 1992]. Its construction enables both 2-D and also full (95% of the unit sphere) 3-D electrons measurements. For most of the mission, the 3-D high-resolution scheme was used. In this mode, electrons are measured in 32 azimuthal and seven polar angle bins within an energy range from 1.6 to 862 eV divided into 20 steps and time resolution of a few minutes. Figure 3 shows one of the measured 3-D eVDFs projected in the ($v_\perp$, $v_\parallel$) plane, $\perp$ and $\parallel$ with respect to the local magnetic field direction. The dots represent the measured bins which are again interpolated to a grayscale map.

[11] Other necessary plasma parameters needed for our study, e.g., ion density, solar wind bulk speed, and the ambient magnetic field, are taken from data products resulting from measurements made by the corresponding plasma instruments on board these three spacecraft.

3. Electron VDF Fitting Method

[12] We estimate the temperature anisotropy of the electron velocity distribution functions using a fitting of the distribution functions with an analytical model. By doing so, we obtain directly the second order moments of the eVDFs corresponding to the parallel and perpendicular temperatures. Electrons in the solar wind typically consist of three different populations: a nearly isotropic thermal core, representing roughly 95% of the total density; a suprathermal halo; and a magnetic field-aligned strahl. Besides some preliminary attempts to model the strahl [e.g., *Pagel et al.*, 2007], this component has still not been fully analytically described. It is not easy to fit this component in/separately from the rest of the distribution. To model the observed eVDFs, we use therefore only a core-halo model

$$f_M = f_c + f_h, \tag{1}$$

where f_c and f_h correspond to the core and halo component of the eVDF, respectively. Furthermore, for the fit we use only those data points that are measured in the sunward direction where the strahl is usually not observed (assuming that the core and halo populations have the same properties in the antisunward direction). We have also removed data points below the one count level. The core population is well described with a bi-Maxwellian distribution function

$$f_c = A_M \exp\left[-\frac{m}{2k}\left(\frac{1}{T_{c\perp}}v_\perp^2 + \frac{1}{T_{c\parallel}}v_\parallel^2\right)\right], \tag{2}$$

where n_c is the core density, m is the electron mass, k is the Boltzmann constant, and $T_{c\perp}$ and $T_{c\parallel}$ are the core perpendicular and parallel temperatures, respectively. The normalization factor A_M is equal to

$$A_M = n_c\left(\frac{m}{2\pi k}\right)^{3/2}\frac{1}{T_{c\perp}}\frac{1}{\sqrt{T_{c\parallel}}}. \tag{3}$$

Contrary to the classical model by *Feldman et al.* [1975] consisting of a sum of two bi-Maxwellians, *Maksimovic et al.* [2005] have shown that the halo component is best modeled by a bi-Kappa distribution function

$$f_h = A_\kappa\left(1 + \frac{m}{k(2\kappa-3)}\left(\frac{1}{T_{h\perp}}v_\perp^2 + \frac{1}{T_{h\parallel}}v_\parallel^2\right)\right)^{-\kappa-1}, \tag{4}$$

where n_h is the halo density and $T_{h\perp}$ and $T_{h\parallel}$ are the halo perpendicular and parallel temperatures, respectively. Ac-

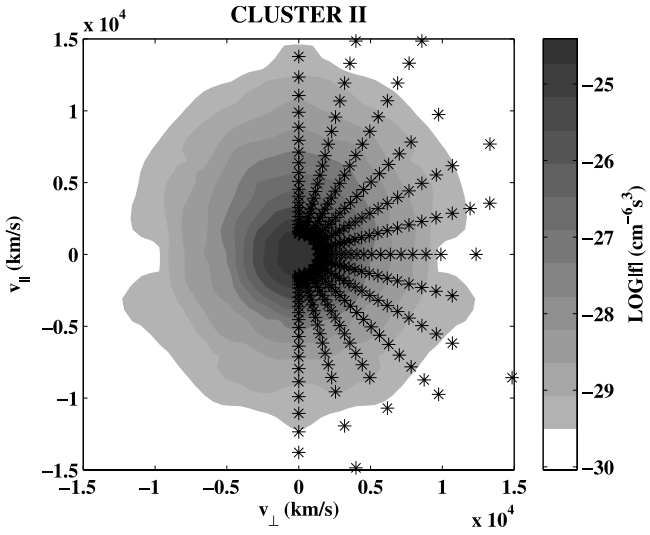

Figure 2. Example of SPINPAD data product obtained by PEACE on board Cluster II. The values (asterisks) are interpolated with a grayscale map.

tually these are not exactly the thermodynamic temperatures but the corresponding second-order moments of the eVDF. The parameter κ in (4) represents the importance of the high-energy nonthermal tails (for $\kappa \to \infty$ the distribution tends to bi-Maxwellian). The normalization factor in this case is equal to

$$A_\kappa = n_h \left(\frac{m}{\pi k (2\kappa - 3)} \right)^{3/2} \frac{1}{T_{h\perp}} \frac{1}{\sqrt{T_{h\|}}} \frac{\Gamma(\kappa + 1)}{\Gamma(\kappa - 1/2)}. \quad (5)$$

Assuming the decomposition (1) of the VDF where the two components are given by (2) and (4), respectively, we have seven parameters to fit, n_c, n_h, $T_{c\perp}$, $T_{c\|}$, $T_{h\perp}$, $T_{h\|}$, and κ. Instead of fitting f_M directly, we fit the logarithm of the distribution function, $\log f_M$, to take account for the high-energy part of the eVDFs, which is some orders of magnitude smaller than the core. Since our model eVDF depends nonlinearly on the fit parameters, we use an iterative fitting technique based on the well-known Levenberg-Marquardt algorithm [*Marquardt*, 1963] to minimize the χ^2 function. To better compare all fits, we also computed a standard-error-like parameter defined by

$$\epsilon = \sqrt{\frac{\chi^2}{N - 1}}, \quad (6)$$

where N is the number of fitted points for corresponding data sample and ϵ serves as indicator of the good quality of the fit.

[13] Typically, the measured eVDFs are influenced by several effects and some corrections must be performed before applying the fitting procedure. First of all, the measured eVDFs are modified by the S/C potential by which the solar wind electrons energy is changed and therefore the computed moments of the eVDFs are modified [see *Song et al.*, 1997]. However, if we assume that the S/C potential is roughly isotropic around the spacecraft, the ratio $T_\perp/T_\|$ for the bi-Maxwellian distribution will remain unaffected. For the bi-kappa function representing the VDF of the halo electrons the temperature is modified. However, since the measured bins of the halo population lie at higher energies (typically 280 eV) the average S/C potential of 5 V does not change the halo population too much and the error made in the temperature estimation is thus negligible. Therefore we did not consider this effect in this study. In the further analysis we assume the total electron density to be equal to the proton density (quasi-neutrality) as obtained from the ion measurements. Second, the core population is polluted by the cold photoelectrons emitted from the spacecraft body. This part of the eVDF has to be removed from the analysis using an energy cutoff. The energy threshold was set to 12 eV in our case. This value should ensure that most of the photoelectrons are removed in the large variety of all data samples while still giving a sufficiently accurate estimation of the core electron temperature. The last thing we have to account for before the fitting is the velocity shift into the solar wind plasma frame. The eVDFs are measured in the spacecraft frame while our model expects plasma at rest. Thus the S/C velocity (usually negligible for the electrons) and the solar wind bulk speed, taken from the ion measurements, have to be subtracted from the measured electron speeds.

[14] Figure 4 is an example of a fit to a Helios I data sample. The asterisks are fitted with the described core/halo model while the dots are not because of the presence of the strahl population or because the data are below the one count level. The solid line represents the sum of the core (dashed line) and halo (dash-dotted line) population. The four panels include cuts along the eight direction measured by Helios. The corresponding pitch angles of these cuts are given in the lower corners. At pitch angles of $-18°$ and $28°$ (upper left and lower right panel) the strahl population is visible.

4. Results

[15] We applied the fitting procedure on roughly 120,000 samples of measured eVDFs. As a measure of the goodness

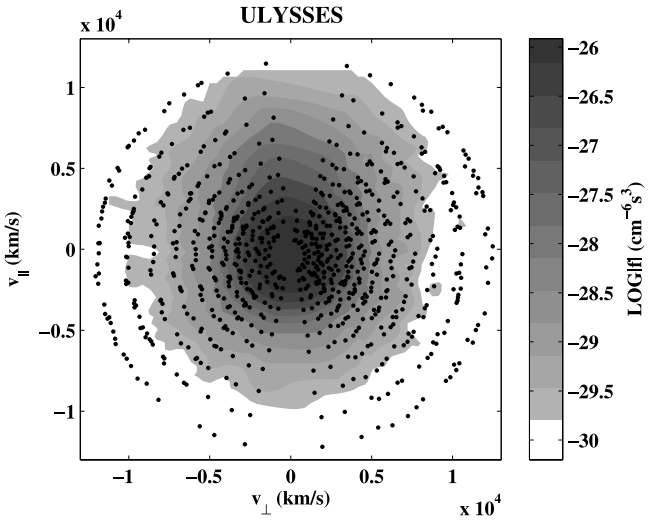

Figure 3. Example of an electron distribution function as it is measured with SWOOPS. The dots represent the measured bins in the velocity space.

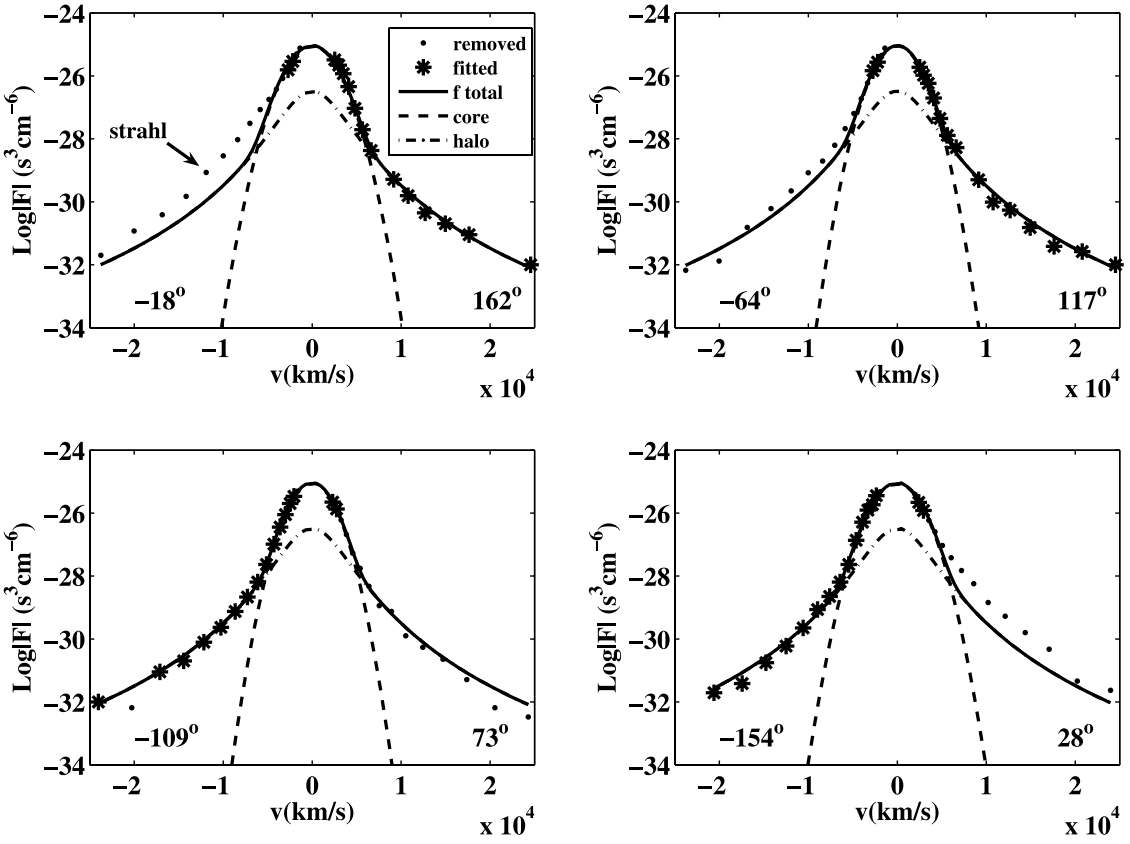

Figure 4. Example of fitted eVDF from Helios measurements. The panels show cuts through the eVDF and the corresponding pitch angles are given in the lower corners of the panels. Points represented by asterisks are fitted while points represent by dots are data which are not taken into account because of the strahl population or the one count level.

of fit, we have used the value of the standard error ϵ defined in (6). For further analysis, we keep only fits where the standard error satisfies

$$\epsilon \leq \mu(\epsilon) + 2/3\, std(\epsilon), \tag{7}$$

where $\mu(\epsilon)$ is the mean value of ε over all eVDF samples and $std(\epsilon)$ is the standard sample deviation from the mean value. This condition was met for ≈85% of all samples. Another 5% of samples were removed from further analysis by reason of unrealistic parameter results. The standard error of the fit of these samples agreed with (7) but the shape of the measured eVDF was considerably different from the typical one and the estimated moments did not correspond to expected conditions in the solar wind (e.g., core temperatures larger than 10^6 K which is comparable to the estimated temperature in the solar corona).

[16] As already mentioned, the fastest growing modes of electron temperature anisotropy instabilities are the whistler and the fire hose instability. For both, the curves of the constant growth rates derived from the linear theory can be approximated by ([*Gary and Wang*, 1996; *Gary and Nishimura*, 2003])

$$\frac{T_\perp}{T_\parallel} = 1 + \frac{a}{\beta_\parallel^b}, \tag{8}$$

where the parameter a is positive for the whistler instability and negative for the fire hose. The appropriate values for the parameters a and b are given in Table 1 of *Gary and Wang* [1996] and Table 1 of *Gary and Nishimura* [2003]. The equation (8) represents a relation between the electron temperature anisotropy and the electron parallel plasma beta and illustrates the importance of the ratio between the particle kinetic and magnetic field pressures.

[17] We compare the curves of constant growth rates of both dominant unstable modes with the electron temperature anisotropy obtained from the fitting process in the ($T_\perp/T_\parallel$, $\beta_\parallel$) space. Results obtained for the thermal core population are shown on Figure 5. The thermal core population is in better agreement with the instability thresholds predicted by the linear theory because it represents the majority of all the electrons and it is well described by single bi-Maxwellian as is assumed in predictions of the linear theory. Results for the slow (upper panel) and fast (lower panel) are presented in Figure 5 separately. For a slow solar wind we considered the samples with electron bulk speed less then 500 km/s and for fast wind we considered samples with bulk speed greater than 600 km/s. The dash-dotted and the dashed line represent the isocontours of growth rates for the whistler and fire hose instability, respectively. The counts of the observed ratio between the core perpendicular $T_{c,\perp}$ and parallel $T_{c,\parallel}$ temperature are represented by a logarithmic grayscale.

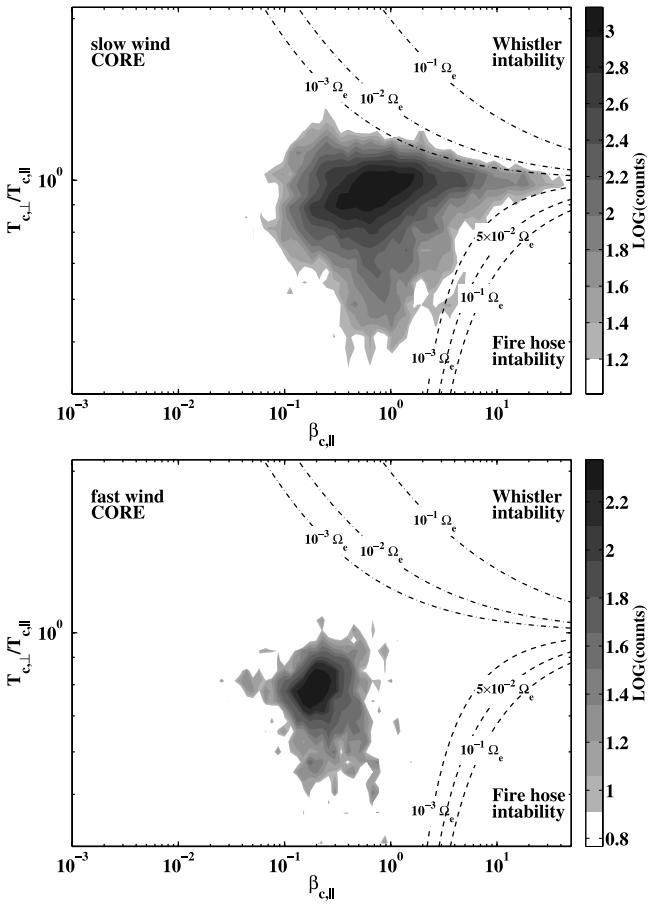

Figure 5. Occurrence rates of the $T_\perp/T_\parallel$ versus $\beta_\parallel$ for the core population in the (top) slow and (bottom) fast solar wind. The curves represent the isocontours of growth rates for the whistler (dash-dotted line) and the fire hose (dashed line) instability.

For higher $\beta_\parallel$, the slow wind is well constrained by the threshold of both the whistler and also fire hose instability. For the fire hose instability, there is still a small gap between the observed plasma conditions and the isocontour of even very low growth rate. This little disagreement between the observations and the linear theory can have its origin in the simplified model used to obtain the predictions based on the linear theory. In the theoretical model we for simplicity assume a single bi-Maxwellian electron distribution while the real electron distributions in the solar wind exhibit more complicated properties including the supra thermal halo and the strahl populations. Deviations from the maxwellian shape of the distribution can modify the predicted shape of the isocontours of the growth rate factors.

[18] For the core population in the fast solar wind the situation is quite different. Here the electron temperature anisotropies are well localized far away from the unstable regions with a mean $T_\perp/T_\parallel$ ratio of 0.75 ± 0.15. This can be explained as a consequence of insufficient number of samples in our data set with an electron bulk speed greater than 600 km/s, which we have selected as a lower limit for the fast solar wind or that the instability thresholds have no relevance in the fast wind. The bulk speed condition for the fast solar wind is satisfied for roughly 10% of Helios and Cluster data while it is less then 1% from all the Ulysses samples. From the theory, confirmed by observations, greater anisotropies develop at larger distances from the Sun. The fact that we do not have sufficient amount of data from larger distances from the Sun can be a reason why we do not see any evolution of the electron temperature anisotropy for the fast solar wind in our data set.

[19] Analogous results for the halo population are shown on Figure 6. The upper and lower panels show results obtained for the slow and fast solar wind, respectively. Note, however, two restrictions in this case. First, the theoretical model used in the linear prediction of the growth rates of the instabilities (bi-Maxwellian) and the analytical model used for the data analysis (bi-Kappa) are different. Second, when computing the theoretical predictions for the halo component, we completely neglect the possible effect of the core. One can thus expect disagreement between the results predicted by the theoretical model and the results based on the analysis of real data. The isocontours of growth rate are here plotted mainly for better comparison

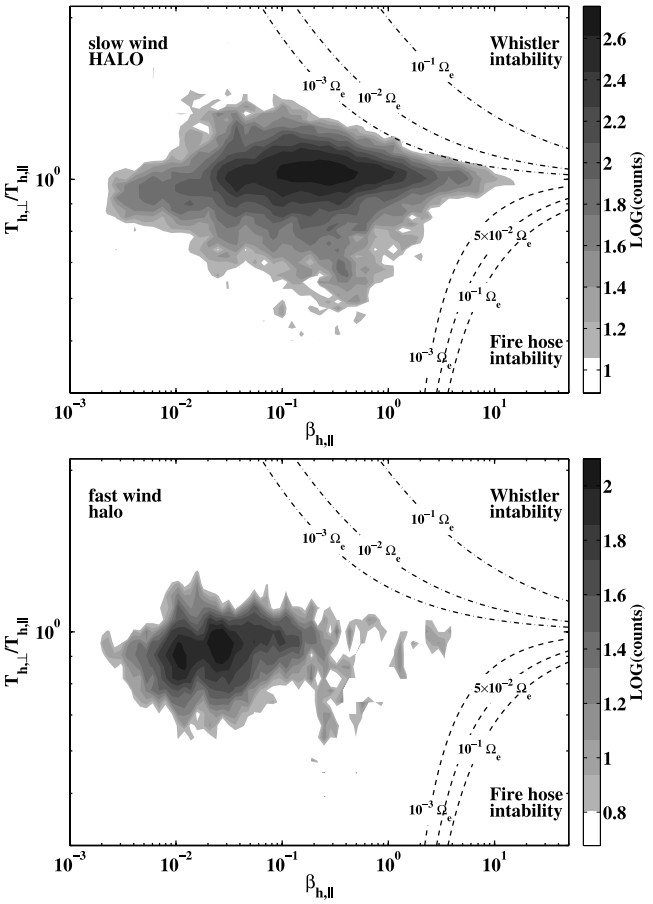

Figure 6. Counts histogram of the $T_\perp/T_\parallel$ versus $\beta_\parallel$ for the halo population in the (top) slow and (bottom) fast solar wind. The curves represent the contours of constant growth rates for the whistler (dash-dotted line) and the fire hose (dashed line) instability. Here the theoretical model does not correspond to the analytical model used for the data analysis.

Table 2. Variation Exponent of the Electron Temperature α Differs for the Slow and the Fast Solar Wind and Depends Also on the Electron Population (Core/Halo)[a]

	Core	Halo
Slow wind	0.5	0.5
Fast wind	0.6	0.3

[a]For this study we have used values displayed in this table.

with Figure 5. Nevertheless, results obtained for the halo population are similar to results of the core population. We find the electron anisotropy close to the constraints predicted by the linear theory in the case of the slow solar wind. In the case when $T_\perp > T_\parallel$ the data are almost consistent with the growth rates of the whistler instability predicted for a bi-Maxwellian. In the opposite of $T_\perp > T_\parallel$, similar processes to the fire hose instability seem to take an effect. If we would use a bi-Kappa rather than a bi-Maxwellian distribution for the computation of the instability threshold, we maybe find the result closer to the observations. This will be the scope of future study. For the fast wind we observe the plasma again in the stable region.

[20] In the following we shall examine the effect of Coulomb collisions which also can participate in exchanging of internal kinetic energy between the plasma particles. Since our data were sampled at different radial distances, we have compared the temperature anisotropy with the electron collisional age A_e [*Salem et al.*, 2003]. The advantage of expressing the effect of Coulomb collisions by the collisional age is that it does not only take into account the current in situ properties of the plasma but it also in a certain manner reflects the time already spent during the expansion of the solar wind from the corona. The collisional age is obtained by integrating the collision frequency from some initial distance up to location of the measurement. The density and temperature heliospheric gradients are assumed to be given by the power laws r^{-2} and $r^{-\alpha}$, respectively. This computation supposes electrons expanding along open magnetic field lines with a constant flow speed. It does not therefore distinguish trapped electrons bouncing back and forth on closed trajectories which already spent more time in the expanding solar wind. The formula for the electron collisional age reads

$$A_e = \nu_{e\perp} \frac{R}{v_{sw}} \left(\frac{1 - (R/r_0)^{1-1.5\alpha}}{1.5\alpha - 1} \right). \quad (9)$$

Here R is the radial distance at which the data sample was acquired, r_0 is the initial distance from which we count the collisions, v_{sw} is the solar wind bulk speed, and $\nu_{e\perp}$ represents the total transverse collision frequency of electrons [see *Phillips and Gosling*, 1990] at the place where the data are acquired (thus at the distance R from the Sun). The parameter α in (9) depends on the solar wind properties and it varies for the slow and fast wind and also for the core and halo population [see *Issautier et al.*, 1998; *Maksimovic et al.*, 2000; *Fludra et al.*, 1999; *Marsch et al.*, 1989]. Because of a large number of various studies published on this topic, we have used some average values from all these results. These values of α are displayed in Table 2. The initial distance r_0 was set to 0.2 AU, a small step back from the minimum distance R of our data samples in order to keep the term in the brackets on the right-hand side of (9) positive.

[21] The correlation between the electron collisional age and the temperature anisotropy of the core population is shown on Figure 7. All samples are represented by a grayscale 2-D histogram. The results are in good agreement with our expectations and also with previous results of *Phillips et al.* [1989] and *Salem et al.* [2003]. With increasing number of collisions, the observed electron distribution functions are closer to the isotropic state. We have also divided the resulting A_e into several bins and computed the corresponding mean collisional age (squares) and the standard deviations (triangle error bars) of the temperature ratio. There is a clearly visible trend of the mean temperature anisotropy tending to 1.0 with increasing number of collisions.

[22] We have also examined the electron temperature anisotropy in the frame of instabilities as a function of the radial distance. According to our expectations based on the theory of the expanding solar wind, higher temperature anisotropies are observed at greater distances with parallel temperature exceeding the perpendicular one. Our data set enables us to examine the relation between the electron temperature anisotropy and the parallel plasma beta as a function of the increasing radial distance from 0.3 AU up to almost 4 AU. The radial evolution is presented (for the core population only) on Figure 8. The lines represent contours circumscribing 70% of all samples at a given radial distance. No visible path in the $(T_\perp/T_\parallel, \beta_\parallel)$ plane can be clearly seen. Only a gentle spreading of the temperature anisotropy with increasing distance can be noticed. Since our statistics for the fast solar wind is insufficient, it is more difficult to perform such an analysis in this case.

[23] We have shown that both, the instabilities as well as the Coulomb collisions, can influence the temperature anisotropy of the solar wind electrons. The final question is whether these effects act independently or are somehow correlated. In general higher plasma beta implies more collisions but nearly isotropic electron distributions are also observed for lower beta. Actually these isotropic distributions with low beta are a consequence of the Coulomb collisions rather than instabilities. This correlation of insta-

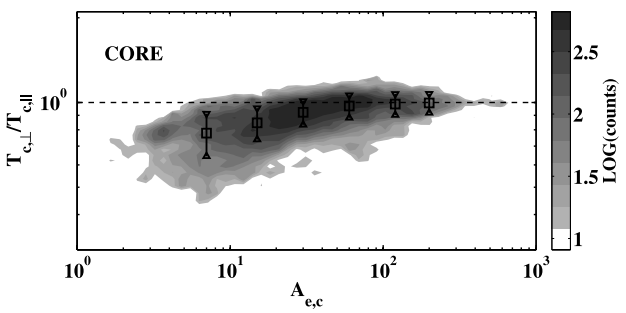

Figure 7. Dependence of the electron temperature anisotropy of the core population on the Coulomb collisions represented by the electron collisional age A_e.

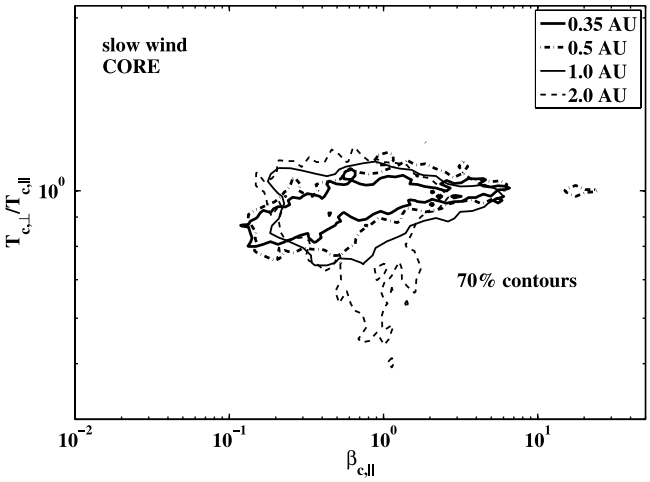

Figure 8. Radial evolution of the core $T_\perp/T_\parallel$ versus $\beta_\parallel$ correlation in the slow solar wind. The lines represent contours circumscribing 70% of all samples at a given radial distance.

bilities and collisions is demonstrated on Figure 9. On this figure all the samples are divided into three bins corresponding to different levels of the electron collisional age. For the bin where collisional age A_e is greater than 60, we find only nearly isotropic electron distributions not only at high electron parallel plasma beta but as well at low values of this parameter. Here the instabilities do not play any role, or are very weak, thus electrons have most likely been isotropized mainly via collisions. The Figure 9 gives another important result. While there was no clear correlation between the temperature anisotropy in the parallel beta frame with increasing radial distance (Figure 8), we can see a nice trend with increasing number of collisions. Instead of a radial trend we may rather speak of a collisional evolution of the temperature anisotropy for the solar wind electrons.

5. Conclusions

[24] In contradiction to the classical CGL relations, the solar wind electrons are typically observed in a nearly isotropic state. We have studied two possible mechanisms which can constrain the electron temperature anisotropy in the solar wind plasma. For this purpose, we have analyzed more than 100,000 electron distribution functions measured on board three different spacecraft, Helios, Cluster, and Ulysses. These observations cover the radial distance from the Sun from 0.3 up to almost 4 AU and were acquired in low ecliptic latitudes only. The electron temperature anisotropy is estimated by fitting of measured electron velocity distribution functions with a core/halo analytical model function. We have then examined the effect of electron temperature anisotropy instabilities and Coulomb collisions and have shown that both, the instabilities as well as Coulomb collisions, influence the temperature anisotropy of the solar wind electrons.

[25] In the case of the slow solar wind having higher electron parallel plasma beta (i.e., $\beta_\parallel \gtrsim 1$), the temperature anisotropy of the core population is well constrained by thresholds of the whistler and fairly well of the fire hose electron instabilities predicted by the linear theory. Similar mechanisms may also act for the non thermal halo component of the solar wind electrons. However, in this case the prediction of the instability thresholds from the linear theory has to be recomputed using a corresponding model for the distribution function. For the fast wind, electron populations are quite well localized far away from unstable regions. Consequently, it is hard to make any conclusions about the electron anisotropy constraints in the fast solar wind, neither for the core nor for the halo population. This is because our statistics in this case is not sufficient. For further studies this part of the data set has to be completed.

[26] Even though the solar wind is usually considered to be a collisionless medium, our results show that electron Coulomb collisions still may have an effect to maintain the temperature anisotropy of the core population. This was demonstrated by use of the electron collisional age and it is in agreement with already published results [*Phillips et al.*, 1989; *Salem et al.*, 2003]. With an increasing number of collisions suffered by electrons the temperature ratio tends to unity.

[27] Since the measurements cover a large range of radial distances, we are also able to examine the radial evolution of the electron temperature anisotropy. We have shown that in agreement with theoretical predictions, greater temperature instabilities can develop at larger distances from the Sun. However, there is no clear evolution of the data in the ($T_\perp/T_\parallel$, $\beta_\parallel$) space as a function of the radial distance. The situation is more interesting if we look at the evolution in the ($T_\perp/T_\parallel$, $\beta_\parallel$) space as a function of collisions. There is a clear trend in the evolution of the core electron populations in dependence upon the collisional age. By virtue of these results, we suggest the core electron Coulomb collisions to be the basic mechanism driving the electron temperature anisotropy of the solar wind electron population. The importance of kinetic instabilities is increasing for higher parallel electron plasma betas.

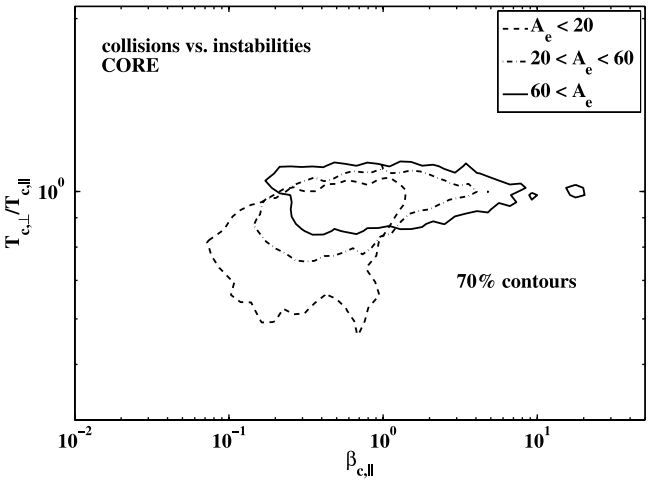

Figure 9. Correlation of electron anisotropy instabilities and electron Coulomb collisions. The electron temperature anisotropy is plotted as a function of the electron parallel plasma beta. All the samples are divided into three bins corresponding to different levels of the electron collisional age.

[28] The electron collisional age used in our study is not the only way to express the importance of collisions in a medium. Furthermore it does not apply to the trapped electrons that circle on closed magnetic field lines. Another way of judging the collision state of the environment is to use the Knudsen number K_n, which is defined as the ratio between the mean free path and the typical density or temperature scale height of the medium [see, e.g., *Maksimovic et al.*, 1997]. In order to verify the conclusions based on the collisional age, we have followed the same analysis of the temperature anisotropy with K_n. The results are qualitatively the same as those for the electron collisional age. This support our conclusions about the effect of collisions on the electron temperature anisotropy.

[29] Finally, it is important to notice that in this study we omitted possible effects of the strahl population. This part of the electron distribution function creates an asymmetry in the parallel direction with respect to the magnetic field. It can thus contribute to the temperature anisotropy for both core and halo electrons and modify in consequence the instability computations. For example, *Saito and Gary* [2007] and *Gary and Saito* [2007] already presented some results based on the particle-in-cell simulations showing interaction of the strahl electrons with whistler waves. It will be thus advisable to take the strahl into account and study the solar wind electrons altogether. To do so, we need a suited analytical description of the strahl which is applicable in the theory and the data processing as well. This will be the scope of a future study.

[30] **Acknowledgments.** SS AND PT acknowledge the support of contract IAA300420602 of the Grant Agency of Academy of Sciences of the Czech Republic and contract PECS 98024 of the European Space Agency. Authors thank Petr Hellinger for useful comments and suggestions.

[31] Amitava Bhattacharjee thanks J. Martin Laming and David Schriver for their assistance in evaluating this paper.

References

Bame, S. J., J. R. Asbridge, W. C. Feldman, J. T. Gosling, and R. D. Zwickl (1981), Bi-directional streaming of solar wind electrons greater than 80 eV: ISEE evidence for a closed-field structure within the driver gas of an interplanetary shock, *Geophys. Res. Lett.*, *8*, 173–176.

Bame, S. J., D. J. McComas, B. L. Barraclough, J. L. Phillips, K. J. Sofaly, J. C. Chavez, B. E. Goldstein, and R. K. Saturai (1992), The Ulysses solar wind plasma experiment, *Astron. Astrophys. Suppl. Ser.*, *92*, 237–265.

Chew, G. F., M. L. Goldberger, and F. E. Low (1956), The Boltzmann equation and the one-fluid hydromagnetic equations in the absence of particle collisions, *Proc. R. Soc. London*, *236*, 112–118.

Dum, C. T., E. Marsch, and W. Pilipp (1980), Determination of wave growth from measured distribution functions and transport theory, *J. Plasma Phys.*, *23*, 91–113.

Escoubet, C., R. Schmidt, and M. Goldstein (1997), Cluster: Science and mission overview, *Space Sci. Rev.*, *79*, 11–32.

Feldman, W., J. R. Asbridge, S. J. Bame, M. D. Montgomery, and S. P. Gary (1975), Solar wind electrons, *J. Geophys. Res.*, *80*, 4181–4196.

Fludra, A., G. Del Zanna, D. Alexander, and B. J. I. Bromage (1999), Electron density and temperature of the lower solar corona, *J. Geophys. Res.*, *104*, 9709–9720.

Gary, S. P., and K. Nishimura (2003), Resonant electron firehose instability: Particle-in-cell simulations, *Phys. Plasmas*, *10*, 3571–3576.

Gary, S. P., and S. Saito (2007), Broadening of solar wind strahl pitch-angles by the electron/electron instability: Particle-in-cell simulations, *Geophys. Res. Lett.*, *34*, L14111, doi:10.1029/2007GL030039.

Gary, S. P., and J. Wang (1996), Whistler instability: Electron anisotropy upper bound, *J. Geophys. Res.*, *101*, 10,749–10,754.

Gary, S. P., E. Neagu, R. M. Skoug, and B. E. Goldstein (1999), Solar wind electrons: Parametric constraints, *J. Geophys. Res.*, *104*, 19,843–19,850.

Gosling, J. T., D. N. Baker, S. J. Bame, W. C. Feldman, R. D. Zwickl, and E. J. Smith (1987), Bidirectional solar wind electron heat flux events, *J. Geophys. Res.*, *92*, 8519–8535.

Hellinger, P., P. Trávníèek, J. C. Kasper, and A. J. Lazarus (2006), Solar wind proton temperature anisotropy: Linear theory and WIND/SWE observations, *Geophys. Res. Lett.*, *33*, L09101, doi:10.1029/2006GL025925.

Hollweg, J. V., and H. J. Volk (1970), New plasma instabilities in the solar wind, *J. Geophys. Res.*, *75*, 5297–5309.

Issautier, K., N. Meyer-Vernet, M. Moncuquet, and S. Hoang (1998), Solar wind radial and latitudinal structure: Electron density and core temperature from Ulysses thermal noise spectroscopy, *J. Geophys. Res.*, *103*, 1969–1979.

Johnstone, A. D., et al. (1997), Peace: A plasma electron and current experiment, *Space Sci. Rev.*, *79*, 351–398.

Kasper, J. C., A. J. Lazarus, S. P. Gary, and A. Szabo (2003), Solar wind temperature anisotropies, in *Solar Wind Ten*, edited by M. Velli et al., *AIP Conf. Ser.*, *679*, 538–541.

Kennel, C. F., and H. E. Petscheck (1966), Limit on stably trapped particle fluxes, *J. Geophys. Res.*, *71*, 1–28.

Li, X., and S. R. Habbal (2000), Electron kinetic firehose instability, *J. Geophys. Res.*, *105*, 27,377–27,386.

Livi, S., E. Marsch, and H. Rosenbauer (1986), Coulomb collisional domains in the solar wind, *J. Geophys. Res.*, *91*, 8045–8050.

Maksimovic, M., V. Pierrard, and J. F. Lemaire (1997), A kinetic model of the solar wind with Kappa distribution functions in the corona, *Astron. Astrophys.*, *324*, 725–734.

Maksimovic, M., S. P. Gary, and R. M. Skoug (2000), Solar wind electron suprathermal strength and temperature gradients: Ulysses observations, *J. Geophys. Res.*, *105*, 18,337–18,350.

Maksimovic, M., et al. (2005), Radial evolution of the electron distribution functions in the fast solar wind between 0.3 and 1.5 au, *J. Geophys. Res.*, *110*, A09104, doi:10.1029/2005JA011119.

Marquardt, D. (1963), An algorithm of least-squares estimation of nonlinear parameters, *J. Appl. Math.*, *11*, 431–441.

Marsch, E. (2006), Kinetic physics of the solar corona and solar wind, *Living Rev. Sol. Phys.*, *3*, 1. (Available at http://www.livingreviews.org/lrsp-2006-1)

Marsch, E., K. M. Thieme, H. Rosenbauer, and W. G. Pilipp (1989), Cooling of solar wind electrons inside 0.3 AU, *J. Geophys. Res.*, *94*, 6893–6898.

Marsch, L., E. Zhao, and C.-Y. Tu (2006), Limits on the core temperature anisotropy of solar wind protons, *Ann. Geophys.*, *24*, 2057–2063.

Paesold, G., and A. O. Benz (1999), Electron firehose instability and acceleration of electrons in solar flares, *Astron. Astrophys.*, *351*, 741–746.

Pagel, C., S. P. Gary, C. A. de Koning, R. M. Skoug, and J. T. Steinberg (2007), Scattering of suprathermal electrons in the solar wind: ACE observations, *J. Geophys. Res.*, *112*, A04103, doi:10.1029/2006JA011967.

Phillips, J. L., and J. T. Gosling (1990), Radial evolution of solar wind thermal electron distributions due to expansion and collisions, *J. Geophys. Res.*, *95*, 4217–4228.

Phillips, J. L., J. T. Gosling, D. J. McComas, S. J. Bame, S. P. Gary, and E. J. Smith (1989), Anisotropic thermal electron distributions in the solar wind, *J. Geophys. Res.*, *94*, 6563–6579.

Pilipp, W. G., K.-H. Muehlhaeuser, H. Miggenrieder, M. D. Montgomery, and H. Rosenbauer (1987a), Characteristics of electron velocity distribution functions in the solar wind derived from the Helios plasma experiment, *J. Geophys. Res.*, *92*, 1075–1092.

Pilipp, W. G., K.-H. Muehlhaeuser, H. Miggenrieder, H. Rosenbauer, and R. Schwenn (1987b), Variations of electron distribution functions in the solar wind, *J. Geophys. Res.*, *92*, 1103–1118.

Porsche, H. (1975), Die helios-sonde als experimententräger, *Raumfahrtforschung*, *19*, 233.

Rosenbauer, H., et al. (1977), A survey on initial results of the Helios plasma experiment, *J. Geophys. Zeitschrift Geophys.*, *42*, 561–580.

Saito, S., and S. P. Gary (2007), Whistler scattering of suprathermal electrons in the solar wind: Particle-in-cell simulations, *J. Geophys. Res.*, *112*, A06116, doi:10.1029/2006JA012216.

Salem, C., D. Hubert, C. Lacombe, A. Mangenay, D. Larson, and L. R. P. (2003), Electron properties and coulomb collisions in the solor wind at 1 au: Wind observations, *Astrophys. J.*, *585*, 1147–1157.

Schwenn, R., H. Rosenbauer, and H. Miggenrieder (1975), Das Plasmaexperiment auf Helios, *Raumfahrtforschung*, *19*, 226–232.

Song, P., X. X. Zhang, and G. Pashmann (1997), Uncertainties in plasma measurements: Effect of lower cutoff energy and spacecraft charge, *Planet. Space Sci.*, *45*, 255–267.

A. N. Fazakerley, Mullard Space Science Laboratory, University College London, Holmbury St. Mary, Dorking, Surrey, RH5 6 NT, UK.

M. Maksimovic, Laboratoire d'Etudes Spatiales et d'Instrumentation en Astrophysique, Observatoire de Paris, Centre National de la Recherche Scientifique, 5 Pl. J. Janssen, Meudon F-92195, France.

E. Marsch, Department for Sun and Heliosphere, Max Planck Institute for Solar System Research, Max-Planck-Strasse 2, Katlenburg-Lindau, D-37191 Germany.

E. E. Scime, Department of Physics, West Virginia University, Box 6315, Morgantown, WV 26506, USA.

Š. Štverák and P. Trávníček, Institute of Atmospheric Physics, Academy of Sciences of the Czech Republic, Bocni II 1401, Prague 14131, Czech Republic. (stverak@alenka.ufa.cas.cz)